Available online at www.sciencedirect.com
SCIENCE DIRECT®
Pergamon
International Journal of Machine Tools & Manufacture 43 (2003) 925–936
INTERNATIONAL JOURNAL OF MACHINE TOOLS & MANUFACTURE
DESIGN, RESEARCH AND APPLICATION

Modeling of waterjet guided laser grooving of silicon

C.-F. Li, D.B. Johnson, R. Kovacevic *

Department of Mechanical Engineering, Research Center for Advanced Manufacturing, Southern Methodist University, 1500 International Parkway, Suite 100, Richardson, TX 75275-0335, USA

Received 18 November 2002; accepted 26 February 2003

Abstract

Waterjet guided laser processing is an internationally patented technique based on guiding a laser inside a thin, high-speed waterjet. The process combines the advantages of laser processing with those of waterjet cutting and offers promise as a method for processing thin and heat sensitive materials with a high degree of precision. An improved understanding of the complex interaction between laser, waterjet, and workpiece is required to enable the process to achieve its potential. A model for waterjet guided laser grooving of silicon is presented that treats the energy input of the laser, the cooling effect of the waterjet, and the melting and removal of the silicon. The thermal process is represented in detail in the new method. The model is validated by comparisons of simulation and experimental results, and the simulation provides insight regarding the details of the interactions among laser, waterjet, and workpiece.

Keywords: Modeling; waterjet; laser; thermal process

1. Introduction

Lasers of different types now are used in a variety of material processing applications for a wide range of materials. Carbon dioxide, Nd:YAG, and Ti:sapphire lasers have been applied in processes including welding, cutting, drilling, grooving, surface treatment, and ablation deposition. There appears to be no limit to the range of possible materials, which include metals, ceramics, composite materials, polymers, semiconductors, and biological tissue. Lasers used in material processing can be continuous wave or pulsed, with pulse widths ranging from milliseconds to femtoseconds.

The development of a process for a specific application is complicated by the multitude of process parameters involved. Historically, satisfactory process parameters for a specific application have been based on empirical knowledge and experience. Due to the increasing use of lasers in commercial production and in the continuing development of new applications, there is significant interest in the development of models that can describe the complex laser–material interactions well enough to guide the selection of process parameters. Since laser material processing is a transient process that involves transmission, absorption, and reflection of radiant energy; conduction, convection, and radiation of thermal energy; temperature-dependent material properties; moving boundaries; melting; fluid flow; vaporization; and gas dynamics; the selection and implementation of an appropriate model is challenging (Fig. 1).

In 1996 Mazumder et al. [1] provided a review of laser materials processing modeling efforts including a list of 135 references and concluded that “a lot remains to be accomplished for the thorough understanding and development of physically realistic models for many laser materials processing applications”. Among their specific observations were that more work is required to relax the limiting approximations of constant thermophysical properties, improve modeling of combined convection and vaporization phenomena, and improve representation of the coupling of heat transfer, resolidification, and solute distribution in the molten pool.

Ganesh et al. [2–4] developed a 2D axisymmetric model with particular emphasis on the treatment of the

* Corresponding author. Tel.: +1-214-768-4865; fax: +1-214-768-0812.
E-mail address: kovacevi@seas.smu.edu (R. Kovacevic).

0890-6955/03/$ - see front matter © 2003 Elsevier Science Ltd. All rights reserved.
doi:10.1016/S0890-6955(03)00063-4

Nomenclature

A	laser heat source term, W/m^3
A_L	heat source term for absorption of latent heat of melting, W/m^3
c_p	specific heat, J/kg K
d	diameter of waterjet guided laser, m
f	pulse frequency, cycles/s
h_c	convection heat transfer coefficient, W/m^2 K
I	laser power intensity, W/m^2
k	thermal conductivity, W/m K
L	thickness, m
L_m	latent heat of melting, J/kg
Nu	Nusselt number
P	laser pulse output, W
Pr	Prandtl number
p	waterjet pressure, N/m^2
Q_m	excess heat sum for a particular element, J/m^3
q	heat flux, W/m^2
R	reflectivity of the material
Re	Reynolds number
T	temperature, K
T_a	ambient temperature, K
T_{im}	imaginary temperature, K
T_m	melting temperature, K
T_{re}	real temperature in the machined region, K
t	time, s
V	speed, m/s
w	subscript used to indicate a property of water
x,y,z	Cartesian system coordinates, m
α	absorption coefficient, m^{-1}
ε	local surface emissivity
μ	dynamic viscosity, kg/m s
ρ	density, kg/m^3
σ	Stephan–Boltzmann constant, W/m^2 K^4
τ	pulse length, s
φ	pressure loss coefficient
$\vec{n}$	unit vector normal to the surface
$\vec{e_z}$	unit vector parallel to the z axis

phase changes associated with melting and resolidification. The volume-of fluid method [5] was used to track the solid–liquid interface, and a 1D gas dynamics model was used to provide the pressure and temperature on the melt surface. Material removal due to vaporization was not taken into account. Good agreement was reported between simulation and experimental material removal rates for holes drilled in Hastelloy-X material with an Nd:YAG laser. In 2000, a 1D heat conduction model was developed by Gutierrez and Jen [6] and used to investigate the effects of temperature-dependent thermal properties. Gutierrez and Jen did not include any consideration of phase changes.

In 1998, Zhang and Modest [7] performed experiments in which they measured the energy required to remove a unit mass of material, or 'heat of removal', during laser drilling of ceramics. Experimental data were obtained for holes drilled in three industrial ceramics by use of millisecond pulsed CO_2 and Nd:YAG lasers and for different power levels. Incident and reflected laser energy as well as the mass of the ablated material were measured, and conduction losses were estimated by use of a numerical model [8]. For the lasers and power levels tested, the heat of removal was not sensitive either to laser wavelength or power level. Zhang and Faghri [9] developed a thermal model of the melting and vaporization phenomena in laser drilling. Important assumptions made were that incident laser energy all is converted into heat at the surface, liquid metal flow is neglected, and material properties are independent of temperature. In

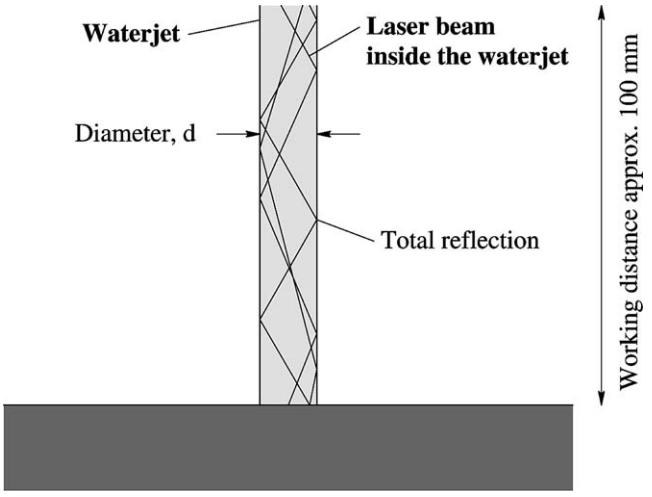

Fig. 1. Schematic mechanism for a waterjet to guide a laser beam [24].

2001, Atanasov et al. [10] reported in a theoretical and experimental study of the use of an Nd:YAG laser with a 10 ns pulse width to drill ceramics. It was assumed for the 1D theoretical model that vaporization occurs in a single step, i.e. that the material is transformed directly from the solid to the vapor phase. Good agreement was found between theoretical and experimental hole depths. Zhang [11] also developed a numerical model for the laser drilling of ceramics. It was assumed that the properties of the ceramic material are independent of temperature in the solid phase and that the ceramic vaporizes in a single step without going through a liquid phase. Zhang simulated the laser drilling of silicon carbide with an Nd:YAG laser having a pulse width of 50 ns and concluded that, for engineering materials with moderate radiation penetration depths, the conduction losses during such short-pulsed laser processing can be quite significant. Ruf et al. [12] developed a simple analytical model for laser drilling for the purpose of revealing the influence of changing surface geometry on ablation rates and Rodden et al. [13] performed experiments to investigate the effect of the use of an assist gas on the Nd:YAG laser drilling of titanium.

Laser cutting of metals is the most common and widely used laser processing application. Nevertheless, reports of efforts to improve the understanding, increase the effectiveness, and extend the capabilities of this well-developed laser process continue to appear [14–18]. The recent research primarily has been directed toward revealing the relationships between cutting speed, assist gas pressure, and type of assist gas on material removal rate and cutting quality.

The relatively recent development of ultra-short pulse lasers, with pulse widths measured in picoseconds or even femtoseconds, as opposed to the continuous wave or millisecond pulse lasers associated with conventional laser processing, also has spurred research. Ultra-short pulse research efforts have been directed toward characterizing the advantages of femtosecond lasers for precise material processing [19]; revealing the relationship between laser fluence and the depth and bottom structure of the hole [20]; the determination of the optimum pulse width, and the development of effective methods of laser beam delivery [21]; the determination of ablation depth associated with a single laser pulse, and the determination of the threshold fluence for the ablation of aluminum and silicon [22]; and the use of transmission electron microscopy to quantify the extent of the heat affected zone [23].

In 1997, a module for coupling a laser beam with a waterjet was patented by scientists at the Swiss Federal Institute of Technology. As shown in Fig. 1, the coupling module takes advantage of the fact that a ray of light will follow a liquid stream due to the total internal reflection of light at the water–air interface, a phenomenon discovered in 1842 by the French physicist Jacques Babinet. The Swiss company Synova manufactures laser systems based on the water jet guided laser technique [24–26]. The waterjet guided laser combines the advantages of both waterjet and laser processing. However, the water–laser–material interactions associated with the process are not well understood, and no models have appeared in the literature. The subject of the present work is the development and experimental validation of a model for waterjet guided laser grooving of silicon.

2. Modeling of waterjet guided laser grooving

The workpiece is a silicon plate of thickness L, with its top surface in the $z = 0$ plane. The plate is exposed at time $t = 0$ to the waterjet guided laser. Fig. 2 schematically illustrates the coordinate system and workpiece feeding mode.

To evaluate the evolution of the temperature field and the propagation of the groove, the time-dependent heat conduction equation is solved in the workpiece domain subject to the appropriate boundary conditions. The governing equation written in terms of temperature T is

$$\frac{\partial(\rho c_p T)}{\partial t} = \nabla[k(T)\nabla T] + A + A_L \tag{1}$$

where ρ is density, c_p the heat capacity, t the time, k the heat conductivity, A the laser heat source term, and A_L appears as a heat source term when energy associated with the latent heat of melting is being absorbed. For a 3D Cartesian coordinate system, Eq. (1) can be written as

$$\frac{\partial(\rho c_p T)}{\partial t} = \frac{\partial}{\partial x}\left[k(T)\frac{\partial T}{\partial x}\right] + \frac{\partial}{\partial y}\left[k(T)\frac{\partial T}{\partial y}\right] \tag{2}$$

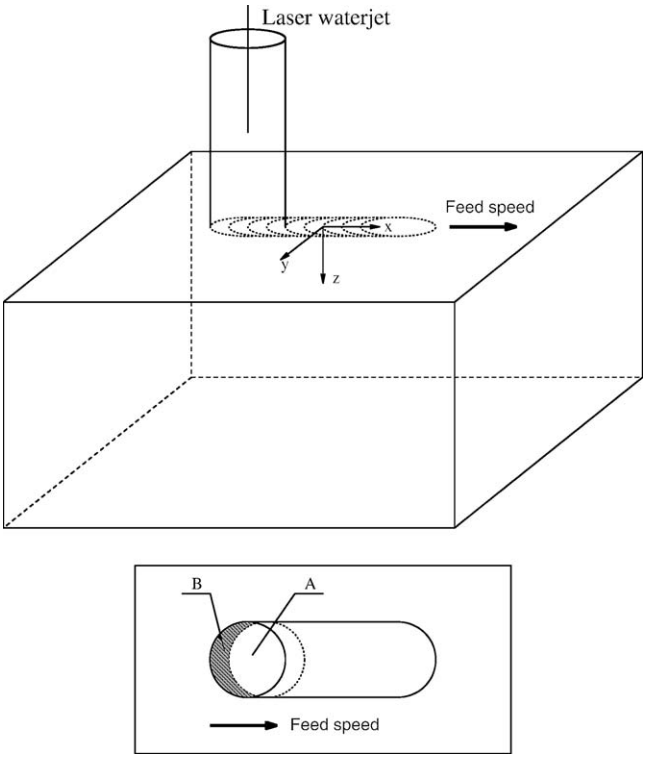

Fig. 2. Schematic depiction of coordinates and feeding mode.

$$+\frac{\partial}{\partial z}\left[k(T)\frac{\partial T}{\partial z}\right]+A+A_{\mathrm{L}}$$

An explicit solution scheme is used in the simulation, with central difference approximations for the spatial derivatives and a forward difference approximation for the time derivative. The temperature of a given volume element after a specific time step is therefore found explicitly from the known current temperatures of the element and its neighbors. Short time increments are required for explicit schemes in order to obtain stability and accuracy. The stability criterion for this explicit scheme is [27,28]

$$1-\left[\frac{2k_x}{\rho c_{\mathrm{p}}(\Delta x)^2}+\frac{2k_y}{\rho c_{\mathrm{p}}(\Delta y)^2}+\frac{2k_z}{\rho c_{\mathrm{p}}(\Delta z)^2}\right]\Delta t\geq 0 \tag{3}$$

which for an isotropic material and a uniform grid can be written simply as

$$\Delta t\leq\frac{\rho c_{\mathrm{p}}(\Delta x)^2}{6k} \tag{4}$$

Since the heat conductivity $k(T)$ is a function of temperature, careful attention must be paid to the discretization of a conduction term such as $\partial/\partial x[k(T)(\partial T/\partial x)]$ in order to satisfy energy conservation. The grid points and cell surfaces are shown in Fig. 3. In finite difference form, $\partial/\partial x[k(T)(\partial T/\partial x)]$ can be written using three consecutive grid points x_{i-1}, x_i, x_{i+1} as

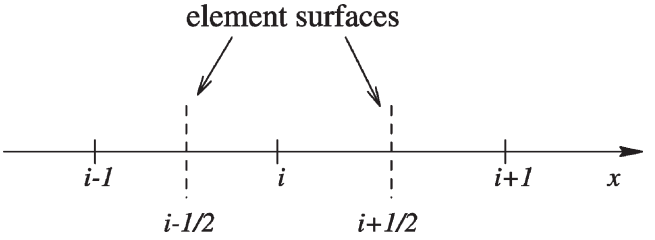

Fig. 3. Grid points in x-direction.

$$\frac{\partial}{\partial x}\left[k(T)\frac{\partial T}{\partial x}\right]_i=\frac{k_{i+1/2}\dfrac{T_{i+1}-T_i}{x_{i+1}-x_i}-k_{i-1/2}\dfrac{T_i-T_{i-1}}{x_i-x_{i-1}}}{x_{i+1/2}-x_{i-1/2}} \tag{5}$$

where two values of the heat conductivity, $k_{i+1/2}$ and $k_{i-1/2}$, have been introduced. The heat flux $q_{i-1/2}$ from x_i to x_{i-1} is

$$k_{i-1/2}\frac{T_i-T_{i-1}}{x_i-x_{i-1}}$$

which also can be expressed as

$$q_{i-1/2}=\frac{T_i-T_{i-1}}{\dfrac{x_i-x_{i-1/2}}{k_i}+\dfrac{x_{i-1/2}-x_{i-1}}{k_{i-1}}} \tag{6}$$

With uniform grid spacing, Eq. (6) yields

$$k_{i-1/2}=\frac{2k_{i-1}k_i}{k_{i-1}+k_i} \tag{7}$$

which has been called harmonic averaging [28]. In the present simulation with non-uniform thermal conductivity distribution, the heat flux across the face between two finite difference cells is calculated by the use of harmonic averaging, rather than by use of arithmetic averaging, so that energy conservation is guaranteed.

The following assumptions relate to the laser energy input, the effect of the waterjet, and the temperature-dependent material properties:

1. The laser power intensity at the workpiece is uniform throughout the cross-section of the waterjet guided laser. Because of the difference between the index of refraction of water and that of air, the laser beam is totally reflected at the air–water interface. After many reflections, the assumption of uniform laser power intensity at the workpiece is appropriate for waterjet guided laser processing, instead of the assumption of a Gaussian distribution that is widely used for traditional laser processing.
2. The material melting temperature is the maximum temperature reached in the workpiece. The melting and removal of material occurs element-by-element. After an element of the material has reached the melting temperature and also has absorbed additional incoming energy equal to the latent energy of melting,

the element melts and is removed by the action of the waterjet.

3. The fluid dynamics of the waterjet removal of molten material is not considered.
4. The large temperature gradients generated by the intensive laser heat source result in significant thermal property variations. The thermal conductivity k and specific heat c_p of silicon are modeled as functions of temperature T as follows [29,30]:

$$k(T) = \frac{A}{T-B}\ (\mathrm{W/m\ K}) \tag{8}$$

where $A = 29{,}900$, $B = 99$, and T is expressed in K;

$$\rho c_p(T) = (1.4743 + 0.17066T/300) \times 10^6\ (\mathrm{J/m^3\ K}),\quad \text{for } T < 1683\ \mathrm{K} \tag{9a}$$

and

$$\rho c_p(T) = 2.432 \times 10^6\ (\mathrm{J/m^6\ K}),\quad \text{for } T > 1683\ \mathrm{K}. \tag{9b}$$

The constant density value of $\rho = 2330\ \mathrm{kg/m^3}$ is used.

5. Detailed, temperature-dependent expressions for surface reflectivity and absorption coefficient, the optical parameters of interest, are not required.

The general laser heat source $A(z,t)$ can be expressed as

$$A(z,t) = I(t)[1-R(T)]\alpha(T)\ \mathrm{e}^{-\alpha(T)z}\lfloor \vec{n}\vec{e}_z \rfloor \tag{10}$$

where I is the laser power intensity, R the reflectivity of the material, α the absorption coefficient, z the distance measured from the surface, $\vec{n}$ a unit vector normal to the surface, and $\vec{e}_z$ is a unit vector parallel to the z axis. The laser power intensity is given by $I(t) = P(t)/(\pi d^2/4)$, where P is the laser power output and d is the diameter of the waterjet guided laser beam. The rectangular wave shape of the laser power output $P(t)$ is sketched in Fig. 4, where τ is pulse length, and f is pulse frequency. The laser beam may reflect multiple times after it enters the waterjet, and very little energy is allowed to escape. Consequently, independent of the reflectivity of the material, the laser energy in the waterjet is nearly totally absorbed by the silicon workpiece. Therefore, a value of zero can be assumed for the surface reflectivity, eliminating the need for a temperature-dependent expression. With the reflectivity assumed to be zero, the expression for A reduces to

$$A(z,t) = I(t)\alpha\ \mathrm{e}^{-\alpha z}\lfloor \vec{n}\vec{e}_z \rfloor \tag{11}$$

The simulation begins with the use of a volumetric heat source according to the preceding equation, with a constant value for the absorption coefficient α. The absorption coefficient does not change significantly with temperature until it increases greatly when the melting temperature is reached. When the temperature of a surface element reaches the melting temperature, the subsequent laser heat input no longer is modeled as a volume heat source, but instead is modeled as a surface heat flux according to

$$q_{in} = I(t)\lfloor \vec{n}\vec{e}_z \rfloor \tag{12}$$

Consequently, a temperature-dependent expression for the absorption coefficient is not required.

Convection and radiation heat losses take place at the top and bottom surfaces of the workpiece, and the energy losses at these boundaries are calculated by the use of

$$q_{out} = h_c(T-T_a) + \varepsilon\sigma(T^4-T_a^4) \tag{13}$$

where h_c is the convection coefficient, T_a the ambient temperature, σ the Stephan–Boltzmann constant, and ε is the local surface emissivity. The side surfaces of the workpiece are well beyond the region that is significantly heated during the grooving process and are assumed to be insulated.

One of the most important characteristics of waterjet guided laser processing is the high cooling effect of the waterjet. The heat transfer coefficient required to model the waterjet cooling effect for the current simulation is obtained from empirical Nu formulas reported in a review article by Webb and Ma [31], in which the results of many liquid jet heat transfer experiments were summarized. Webb and Ma observed that the stagnation Nu depends approximately on Pr^n where n varies between 1/2 at a small Pr to 1/3 at a large Pr and recommended the following formulas

$$Nu = 0.715Re^{1/2}Pr^{0.4},\quad 0.15 < Pr < 3 \tag{14a}$$

$$Nu = 0.797Re^{1/2}Pr^{1/3},\quad Pr > 3 \tag{14b}$$

The heat transfer coefficient associated with the waterjet cooling effect is calculated by use of Eqs. (14a) and (14b). For liquid water ranging from 0 to 100 °C, the Pr ranges from about 13.0 down to 1.7. Since the heating of the specimen is confined to the stagnation zone, the heat transfer in the radial flow regions is negligible since the waterjet and the specimen initially are at the same temperature. Consequently, it is not necessary to know the Nu in the radial flow regions.

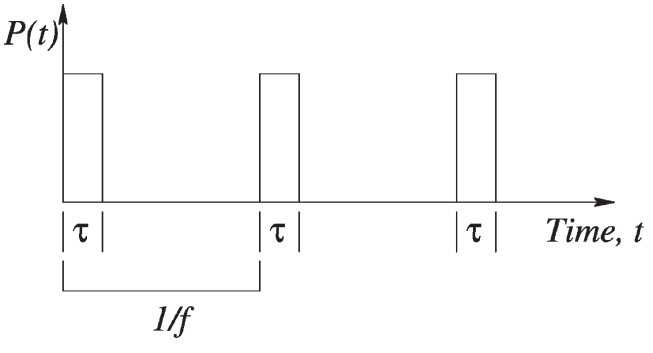

Fig. 4. Laser pulse output.

After the temperature of any element of the workpiece has reached the melting temperature, the additional heat absorbed by the element, instead of increasing the element temperature, is accumulated until it equals the latent heat of melting for the element. After each time step, the temperature of any element whose temperature exceeded the melting temperature during the step is reset to the melting temperature, and the excess heat is added to an accumulating sum for the element concerned. When this sum reaches the level needed to melt the element, the phase transformation is assumed to occur; the molten material is assumed to be removed by the waterjet; the element is not included in subsequent calculations, and the new machined surface moves to the next element. The melting routine can be expressed mathematically as

$$Q_{\mathrm{m}} = \sum_{n_1\Delta t}^{n_2\Delta t} \rho c_{\mathrm{p}}(T_{i,j,k} - T_{\mathrm{m}}) \tag{15}$$

where Q_{m} is the excess heat sum for a particular element, T_{m} the melting temperature, and $n_1\Delta t$ is the time at which the melting temperature is reached. At some later time $n_2\Delta t$, the sum Q_{m} reaches the value of the latent heat of melting for the element; melting occurs, and the element is removed by the waterjet.

As melted material is removed, a machined region is formed in the workpiece. The machined region deepens and widens during processing, so the machined surface is a moving boundary. On the machined surfaces, convection boundary conditions are applied. For computing convenience, a special technique is used to transform the convection boundary conditions to a conductive diffusion form, as sketched in Fig. 5 for a 1D case in the x-direction. According to Fourier's law of heat conduction and Newton's law of cooling, the heat transfer balance across the surface is determined by

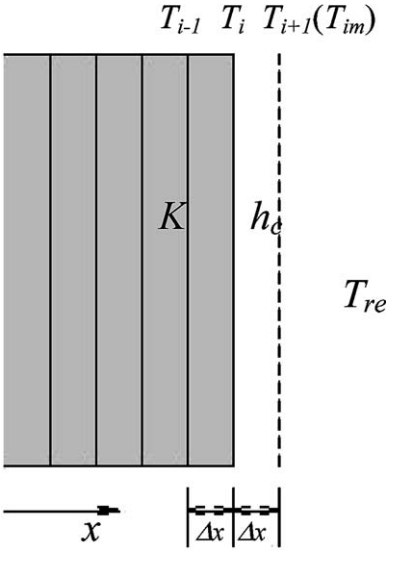

Fig. 5. Imaginary temperature $T_{\mathrm{im}} = T_{i+1}$.

$$-k\left.\frac{\partial T}{\partial x}\right|_{\mathrm{wall}} = h_{\mathrm{c}}(T_i - T_{\mathrm{re}}) \tag{16}$$

where T_{re} is the real temperature in the machined region. The finite difference expression for the derivative can be written as

$$-k\left.\frac{\partial T}{\partial x}\right|_{\mathrm{wall}} = k\frac{T_i - T_{i+1}}{\Delta x}$$

If the machined region is to the right of the element, there is no material at i+1, and T_{i+1} is referred to as the imaginary temperature T_{im}. Thus, the finite difference form of the heat transfer balance is

$$k\frac{T_i - T_{\mathrm{im}}}{\Delta x} = h_{\mathrm{c}}(T_i - T_{\mathrm{re}}) \tag{17}$$

An expression for T_{im} can be found by rearranging the above equation, which leads to

$$T_{\mathrm{im}} = T_i - \frac{h_{\mathrm{c}}\Delta x}{k}(T_i - T_{\mathrm{re}}) \tag{18}$$

where $h_{\mathrm{c}}\Delta x/k$ is the Biot number. Therefore, the convection boundary condition is used to determine an expression for $T_{\mathrm{im}} = T_{i+1}$, which is required for the solution of the temperature diffusion equation. As the solution proceeds and the groove is created, convection boundary conditions are applied as needed to develop expressions for temperatures at points just outside the changing boundary of the machined region.

3. Simulation and experimental results

The new model is used to obtain simulation results for waterjet guided laser grooving of silicon for feed speeds of 0, 5, 50, 100, and 150 mm/s. Comparisons between the simulation results and experimental results obtained by use of the Synova Laser Microjet machine are made for groove depth, shape of vertical cross-section normal to the groove, and groove shape at the surface of the workpiece. Detailed information about the process of waterjet guided laser grooving revealed by the simulation also is presented. The influence of feed speed on the shape of the cross-section parallel to the groove, the temperature distribution and associated groove profile at different instants during the grooving process, and the pulse-by-pulse changes that occur during the initial stage of the process are illustrated.

The laser parameters used include a pulse length of 0.2 μs; a frequency of 25,000 Hz; a laser beam diameter of 50 μm, and laser power intensity at the workpiece of 3.61 TW/m^2. For the low feed speed of 5 mm/s, the

movement of the workpiece relative to the waterjet guided laser during one laser period of 40 μs is only 0.2 μm, which is one-tenth of the finite difference grid spacing. Therefore, 10 laser pulses occur in each finite difference cell for the 5 mm/s feed speed. For the feed speed of 100 mm/s, one laser pulse occurs in every other cell. The waterjet parameters include a pressure of 300 bar, a nozzle diameter of 50 μm, and a waterjet speed that can be calculated by use of the formula

$$V_w = \varphi\left(\frac{2p_w}{\rho_w}\right)^{1/2}$$

where p_w is the waterjet pressure, ρ_w the water density, and φ is the coefficient of pressure loss, which ranges from 0.95 to 0.99 depending on the nozzle [25]. For a waterjet temperature of 50 °C, the water density ρ_w is 988.8 kg/m^3 resulting in a waterjet speed of about 240 m/s for the pressure of 300 bar.

In order to obtain an appropriate expression for the heat transfer coefficient h_c associated with cooling by the waterjet, the Pr ($Pr = c_{pw}\mu_w/k_w$) and the Re ($Re = \rho_w V_w d/\mu_w$) are required. For a waterjet temperature of 50 °C, the specific heat c_{pw} is 4174 J/kg K; the dynamic viscosity μ_w is 5.62×10^{-4} kg/m s; and the thermal conductivity k_w is 0.664 W/m K. Consequently, the Pr is 3.53, and the Re is 21,113. For these values of Pr and Re, Webb and Ma [31] suggested that the stagnation Nu is given by Eq. (14b), which leads to a value of 2.34 MW/ m^2 K for the heat transfer coefficient h_c.

The thickness of the silicon workpiece is 675 μm, and the silicon material properties are given in Table 1.

The simulated and experimental values of groove depths for feed speeds of 5, 50, 100, and 150 mm/s are shown in Fig. 6. The simulated depth value obtained for the extreme situation of zero feed speed, which corresponds to drilling as opposed to grooving, also is plotted in Fig. 6. Groove depth decreases sharply from 240 to 70 μm as feed speed is increased from 5 to 100 mm/s. For feed speed above 100 mm/s however, groove depth decreases very slowly with increasing feed speed. For the simulation results, a range of depth values rather than a single value is shown for the high feed speeds of 100 and 150 mm/s. At these higher speeds, the bottom of the simulated groove is not flat. Instead, the depth varies over a narrow range along the length of the groove (Fig. 9). Each experimental depth value was determined from a digital image of a view through an optical microscope of a groove cross-section exposed by breaking the workpiece perpendicular to the groove. The shapes of the bottoms of the experimental grooves are not known. Inspection of Fig. 6 reveals that the new simulation for waterjet guided laser grooving produces groove depth values that are in good agreement with experimental depth values over a wide range of feed speeds.

Table 1
Silicon material properties

Property	Value
Density	2330 kg/m^3
Thermal conductivity	Eq. (8)
Specific heat	Eqs. (9a) and (9b)
Melting temperature	1683 K
Latent heat of melting	1.79×10^6 J/kg
Convection heat transfer coefficient	100 W/m^2 K
Absorption coefficient (crystalline)	5.0×10^3 m^{-1}

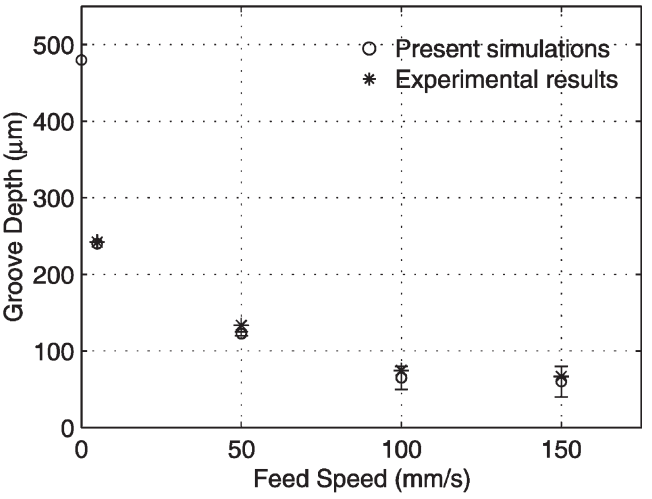

Fig. 6. Simulated and experimental results for groove depth vs. feed speed.

The shape of the vertical cross-section normal to the groove is illustrated in Fig. 7. Simulated and experimental cross-sections for feed speeds of 5 and 100 mm/s are shown in Fig. 7(a) and (b), respectively. For the lower feed speed of 5 mm/s, the depths of the simulated and actual grooves are in excellent agreement, with both being about 240 mm. There is however, a noticeable difference in Fig. 7(a) between the shape of the simulated and experimental cross-sections. For the higher feed speed of 100 mm/s, there is excellent agreement between the simulated and experimental results for both the depth and shape of the cross-section, as shown in Fig. 7(b). It should be noted however, that the bottom of the simulated groove is not flat for the feed speed of 100 mm/s (Fig. 9), with the groove depth varying between 50 and 80 μm. The simulated cross-section selected for Fig. 7(b) has a depth of 80 μm, which corresponds very well with the depth of the actual cross-section shown in Fig. 7(b). The shape of the bottom of the experimental groove and the associated variation of groove depth are not known.

The actual shapes at the workpiece surface of the grooves produced by the Synova Laser Microjet for feed speeds of 5 and 100 mm/s are shown in Fig. 8(a) and (b), respectively. Inspection of Fig. 8 clearly reveals that

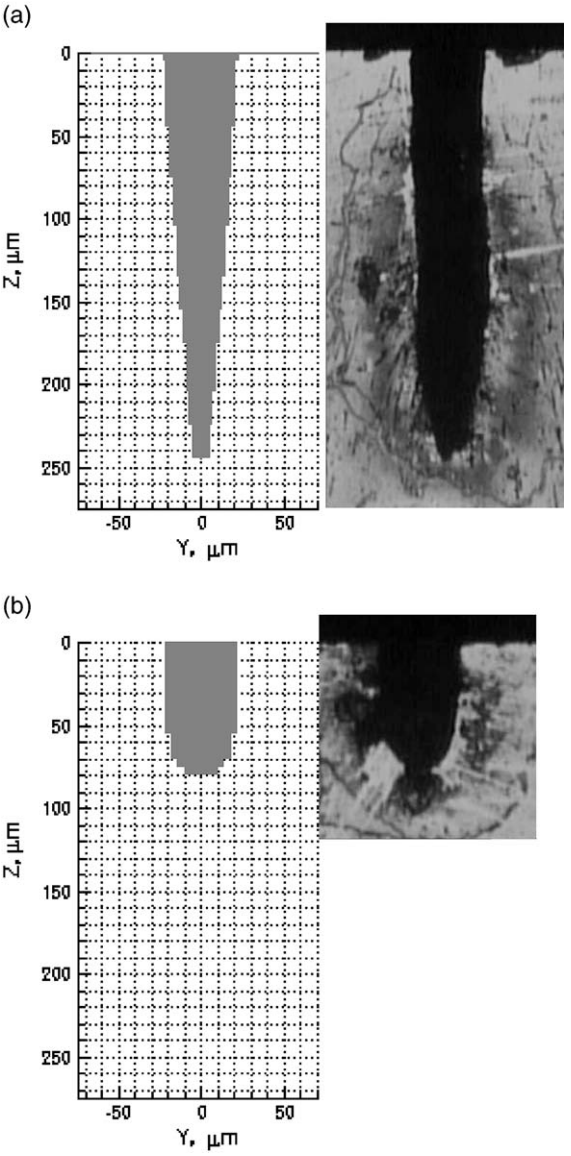

Fig. 7. Simulated and experimental groove cross-sections for feed speeds of (a) 5 mm/s and (b) 100 mm/s.

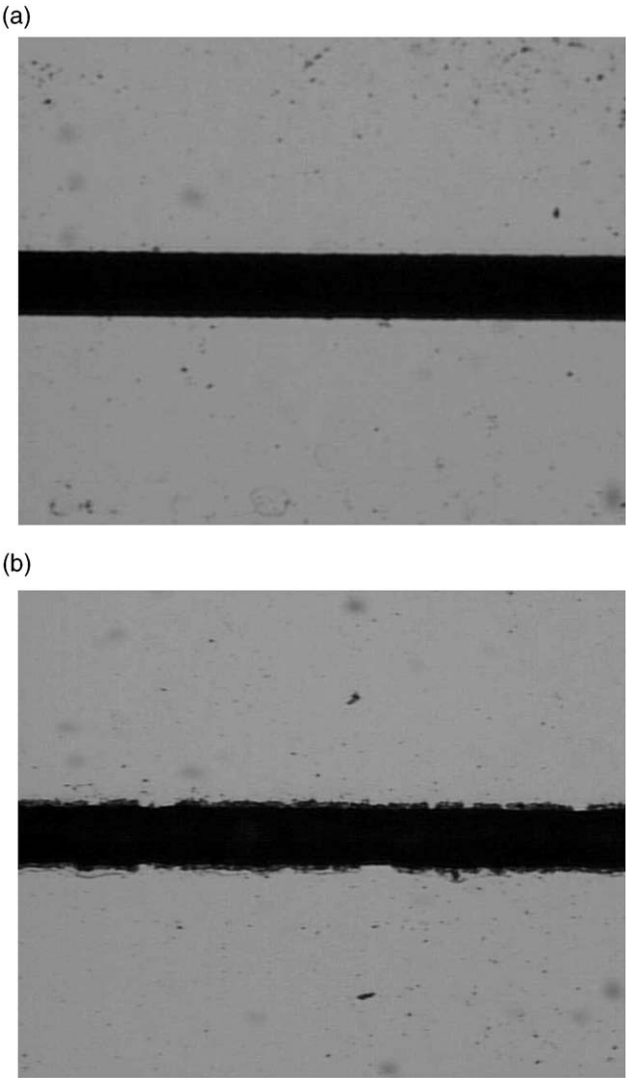

Fig. 8. Top surface views of experimental grooves for feed speeds of (a) 5 mm/s and (b) 100 mm/s.

there is a relationship between feed speed and groove quality. The groove edges produced at the lower speed of 5 mm/s are very straight and smooth compared to the relatively rough groove edges produced at the higher speed of 100 mm/s. The corresponding simulation results are not shown, because for both feed speeds, they are essentially identical to the low speed experimental results shown in Fig. 8(a). Although it correctly predicts the groove width, the simulation fails to reveal the relationship between feed speed and groove quality illustrated in Fig. 8.

For the high feed speed of 100 mm/s, the waterjet guided laser advances 4 μm between one laser pulse and the next. The radius of the laser is 25 μm. If the grid spacing used in the simulation was small enough, it would be possible to observe a variation in the width of the simulated groove of about 0.16 μm for the 100 mm/s feed speed. Since the grid spacing used in the simulation for the *x*- and *y*-directions parallel to the workpiece surface is 2 μm, a variation of 0.16 μm cannot be resolved. However, since the variation of the actual groove width observed in Fig. 8(b) is at least several times greater than 0.16 μm, insufficient grid resolution is not the sole reason that the relationship between feed speed and groove quality is not revealed by the simulation. Some process feature not included in the current model is responsible for the appearance of the rough groove edges at the 100 mm/s feed speed that are observed in Fig. 8(b).

Detailed information about the waterjet guided laser grooving process revealed by the new simulation is presented in Figs. 9–12. The influence of feed speed on the shape of the cross-section parallel to the groove is illustrated in Fig. 9 for feed speeds of 5, 50 and 100 mm/s. The workpiece surface is at $z = 0$, and the center

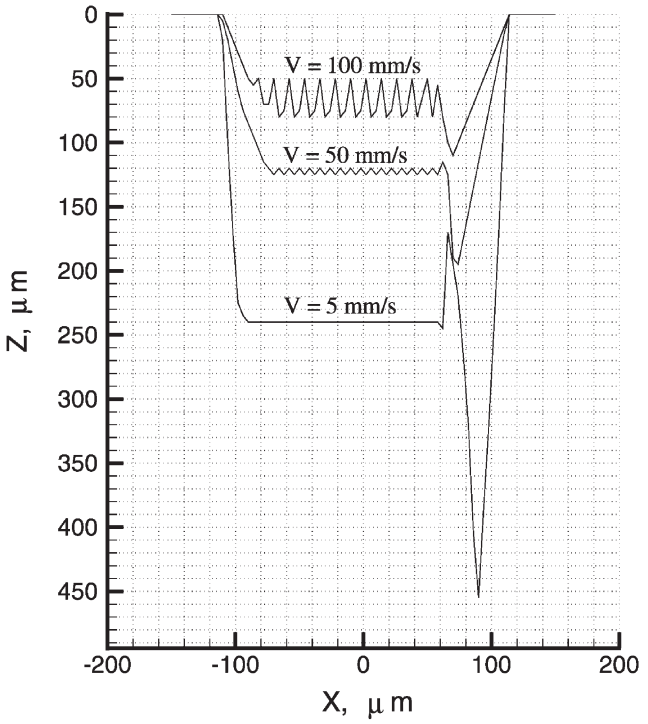

Fig. 9. Groove shape in the central *x–z* plane for different feed speeds.

of the workpiece is at $x = 0$. In Fig. 9, the relative movement of the waterjet guided laser is from right to left. The grooving process is initiated with the axis of the waterjet guided laser positioned at $x = 94$ μm and is terminated with the axis positioned at $x = -86$ μm. In each case, the total travel of the waterjet guided laser is 180 μm. It can be observed in Fig. 9 that the grooving process has reached a steady-state for each speed by the end of the first third of the simulation. Consequently, a total travel distance of 180 μm is more than adequate for the simulation. The total number of laser pulses and the total elapsed time are different for each feed speed as shown in Table 2.

For each feed speed, a groove depth is obtained during the early portion of the process that is greater than the eventual steady-state groove depth. This transient effect is most pronounced at the lowest feed speed and is least pronounced at the highest feed speed. For the feed speed of 5 mm/s, the maximum transient groove depth is about 455 μm. During the early stage of the grooving process at this low speed, the process is somewhat similar to drilling. The drilling depth associated with the laser power intensity of 3.61 TW/m^2 is 480 μm, as shown in Fig. 6. As the waterjet guided laser continues to move, even at the low speed of 5 mm/s, the process resembles drilling less and less, resulting in a steady-state groove depth significantly lower than the early maximum depth.

The steady-state groove depth for the 5 mm/s feed speed is 240 μm, and the bottom of the groove is flat with no perceptible variation in the depth. In contrast, the groove depth for the higher speed of 100 mm/s varies between 50 and 80 μm after the grooving process has reached steady-state. The steady-state variation in groove depth for the intermediate feed speed of 50 mm/s is 5 μm, with the depth ranging between 120 and 125 μm.

The temperature distribution and the groove profile at an instant very early in the grooving process and at the end of the process are displayed in Figs. 10 and 11 for feed speeds of 5 and 100 mm/s, respectively. The view in Figs. 10 and 11 is the same as the view in Fig. 9. Since the final laser pulse is chosen for Figs. 10(b) and 11(b), the associated groove profiles match two of the

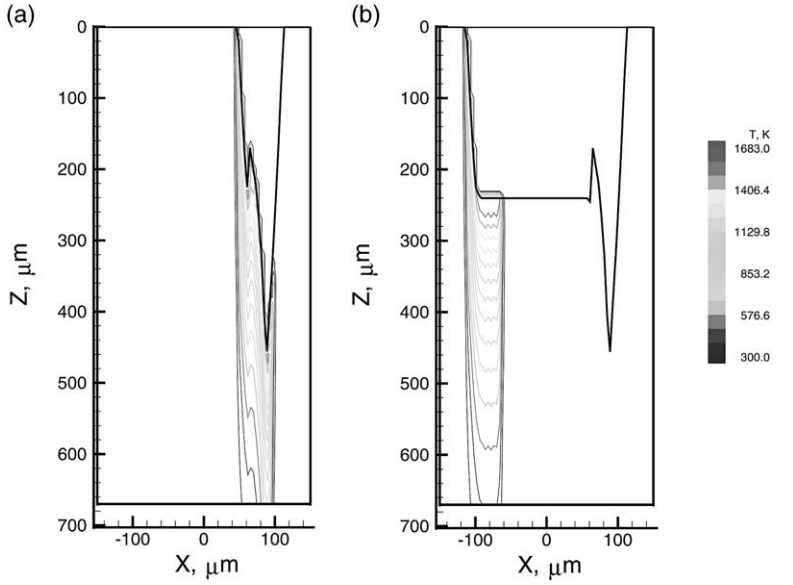

Fig. 10. Temperature distribution and groove profile for feed speed of 5 mm/s after (a) 100 and (b) 900 laser pulses.

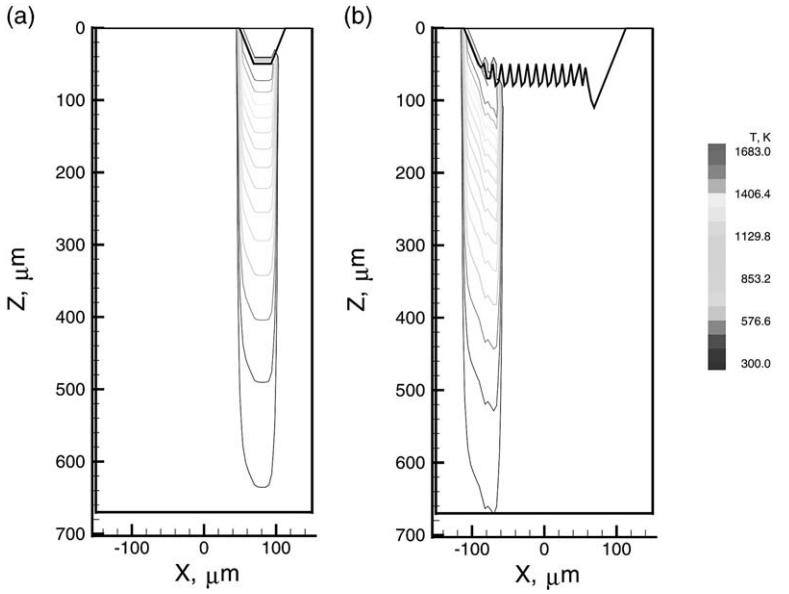

Fig. 11. Temperature distribution and groove profile for feed speed of 100 mm/s after (a) 5 and (b) 45 laser pulses.

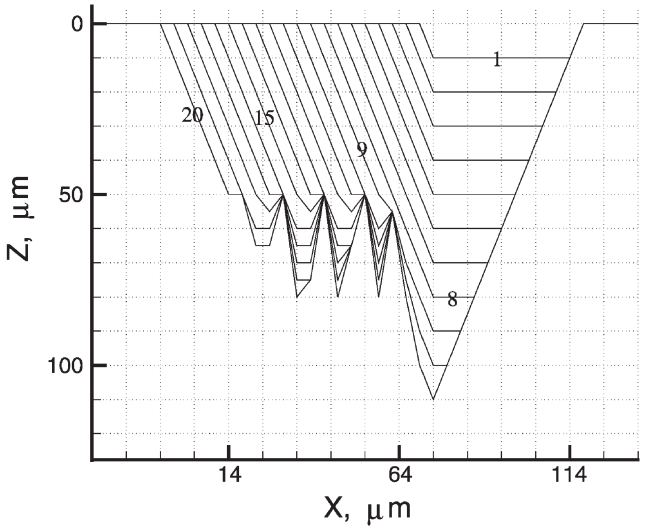

Fig. 12. Groove development during the first 20 pulses for feed speed of 100 mm/s.

Table 2
Number of laser pulses and elapsed time for 180 μm groove at different feed speeds

Feed speed (mm/s)	Number of pulses	Elapsed time (ms)
5	900	36
50	90	3.6
100	45	1.8

completed profiles shown in Fig. 9. Due to the cooling effect of the waterjet, the heat affected zone is very narrow in all four illustrations contained in Figs. 10 and 11. As a result of the high energy input of the laser, the heat affected zones contain high temperature gradients. The maximum temperature of 1683 K in each illustration is found near the edge of the groove profile. In each illustration, the majority of the workpiece remains at the ambient temperature of 300 K.

The temperature distribution and groove profile after 100 laser pulses at the feed speed of 5 mm/s are illustrated in Fig. 10(a). For 5 mm/s, the total number of laser pulses is 900. The axis of the waterjet guided laser beam, which began initially at $x = 94$ mm,, has moved 20 mm and is positioned at $x = 74$ mm after 100 pulses. The temperature distribution and groove profile at the end of the last laser pulse in the grooving process at 5 mm/s are shown in Fig. 10(b).

In Fig. 11(a), the temperature distribution and groove profile after five laser pulses at the feed speed of 100 mm/s are displayed. For 100 mm/s, the total number of laser pulses is 45. The axis of the waterjet guided laser is at the same position for Fig. 11(a) that it is for Fig. 10(a). There are significant differences between the temperature distributions and groove profiles displayed in Figs. 10(a) and 11(a). In particular, the heat affected zone in Fig. 11(a) does not reach the bottom of the workpiece for the feed speed of 100 mm/s, whereas it does in Fig. 10(a) for the much lower feed speed of 5 mm/s.

The complex pulse-by-pulse changes that occur during the initiation of the groove for the 100 mm/s feed speed are shown in Fig. 12. The groove profiles after each of the first 20 laser pulses are displayed. At 100 mm/s, the workpiece moves 4 μm during a single pulse period of 40 μs, which is twice as large as the grid spacing of 2 μm. This 4 μm distance between laser pulses results in the 4 μm horizontal spacing between the series of 20 parallel lines that represent the successive leading

edges of the advancing groove. During the first eight laser pulses, the depth increases by 10 μm per pulse, and the changes in the groove profile follow a uniform pattern. Beginning with the ninth pulse, the nature of the development of the groove changes, and the maximum groove depth occurs during the 11th pulse. During the first few pulses, the boundary conditions are somewhat similar to those for drilling, but by the ninth pulse, a groove has developed and no material surrounds the trailing half of the waterjet guided laser. For a feed speed of 100 mm/s, the grooving process reaches steady-state by the 20th pulse. The section of the groove profile created by pulses 15–20 will be reproduced at a different position during pulses 18–23 and again during pulses 21–26, and so on. The resulting steady-state variation of groove depth between 50 and 80 μm can be observed very clearly in Fig. 9.

4. Conclusions

A model of waterjet guided laser grooving of silicon has been developed. The model has been validated by comparisons of simulated and experimental results. Simulation results for groove depth are in excellent agreement with experimental results over a range of feed speeds from 5 to 150 mm/s. The simulated shape of the groove cross-section perpendicular to the groove also is in excellent agreement with the experimental shape for the feed speed of 100 mm/s. At the much lower speed of 5 mm/s however, there are differences between the simulated and experimental cross-section shapes. For 5 mm/s, the sides of the simulated cross-section are slightly sloped, and the width of the cross-section decreases with depth, whereas the decrease in the width of the experimental cross-section with depth is less pronounced. Excellent agreement exists between the simulated and experimental values of the width of the groove at the surface of the workpiece. The simulation does not predict however, the decrease with increasing feed speed in the quality of the edges of the groove. At the feed speed of 100 mm/s, there is an observable roughness in the edges of the experimental groove in contrast to the straightness of the experimental groove edges at 5 mm/s. The simulation does not reveal this relationship between feed speed and groove quality. In order to capture this relationship, it may be necessary to include in the model the mechanical properties of the workpiece and the momentum effects of the waterjet.

The new model also has revealed details of the process of waterjet guided laser grooving that cannot be compared with experimental results. The influence of feed speed on the shape of the cross-section parallel to the groove is examined. It is found that the steady-state depth of the groove is not constant for feed speeds of 50 mm/s and higher. The steady-state variation in groove depth is only 5 μm at the feed speed of 5 mm/s, but it increases to 30 μm at 100 mm/s. The temperature distribution over the narrow heat affected zone at different stages of the grooving process and for different feed speeds are examined by use of the new simulation. The complex pulse-by-pulse changes that occur as the groove is created, also are examined. The simulation indicates that a maximum depth is reached very early in the grooving process that is larger than the eventual steady-state groove depth.

Acknowledgements

This work was financially supported by the Texas Higher Education Coordinating Board (project no. 003656-00189b-1999) and by the US Department of Education (grant no. P200A80806-98). The authors would like to thank Dr N. Dushkina of the Gem City Engineering Co., Dayton, OH, for providing the experimental data.

References

[1] J. Mazumder, P.S. Mohanty, A. Kar, Mathematical modelling of laser materials processing, International Journal of Materials and Product Technology 11 (3–4) (1996) 193–252.
[2] R.K. Ganesh, W.W. Bowley, R.R. Bellantone, Y. Hahn, A model for laser hole drilling in metals, Journal of Computational Physics 125 (1996) 161–176.
[3] R.K. Ganesh, A. Faghri, A generalized thermal modeling for laser drilling process—I. Mathematical modeling and numerical methodology, International Journal of Heat and Mass Transfer 40 (14) (1997) 3351–3360.
[4] R.K. Ganesh, A. Faghri, A generalized thermal modeling for laser drilling process—II. Numerical simulation and results, International Journal of Heat and Mass Transfer 40 (14) (1997) 3361–3373.
[5] B.D. Nichols, C.W. Hirt, R.S. Hotchkiss, SOLA-VOF: A Solution Algorithm for Transient Fluid Flow with Multiple Free Boundaries, Los Alamos Scientific Laboratory, Los Alamos-8355, 1980.
[6] G. Gutierrez, T.-C. Jen, Numerical simulation of non-linear heat conduction subjected to a laser source: the effects of variable thermal properties, International Journal of Heat and Mass Transfer 43 (2000) 2177–2192.
[7] Z. Zhang, M.F. Modest, Energy requirements for ablation or decomposition of ceramics during CO_2 and Nd:YAG laser machining, Journal of Laser Applications 10 (5) (1998) 212–218.
[8] M.F. Modest, Three-dimensional, transient model for laser machining of ablating/decomposing materials, International Journal of Heat and Mass Transfer 39 (2) (1996) 221–234.
[9] Y. Zhang, A. Faghri, Vaporization, melting, and heat conduction in the laser drilling process, International Journal of Heat and Mass Transfer 42 (1999) 1775–1790.
[10] P.A. Atanosov, E.D. Eugenieva, N.N. Nedialkov, Laser drilling of silicon nitride and alumina ceramics: a numerical and experimental study, Journal of Applied Physics 89 (4) (2001) 2013–2016.
[11] Z. Zhang, Numerical simulation of short-pulsed laser processing of materials, Numerical Heat Transfer, Part A 40 (2001) 497–509.

[12] A. Ruf, P. Berger, F. Dausinger, H. Hügel, Analytical investigations on geometrical influences on laser drilling, Journal of Physics D: Applied Physics 34 (2001) 2818–2925.
[13] W.S.O. Rodden, S.S. Kudesia, D.P. Hand, J.D.C. Jones, Use of "assist" gas in the laser drilling of titanium, Journal of Laser Applications 13 (5) (2001) 204–208.
[14] K. Farooq, A. Kar, Removal of laser-melted material with an assist gas, Journal of Applied Physics 83 (12) (1998) 7467–7473.
[15] S.-L. Chen, The effects of high-pressure assistant-gas flow on high-power CO_2 laser cutting, Journal of Materials Processing Technology 88 (1999) 57–66.
[16] J.M. Prusa, G. Venkitachalam, P.A. Molian, Estimation of heat conduction losses in laser cutting, International Journal of Machine Tools and Manufacture 39 (1999) 431–458.
[17] D. Espinal, A. Kar, Thermochemical modeling of oxygen-assisted laser cutting, Journal of Laser Applications 12 (1) (2000) 16–22.
[18] F. Quintero, J. Pou, F. Lusquiños, M. Larosi, R. Soto, M. Pérez-Amor, Cutting of ceramic plates by optical fiber guided Nd:YAG laser, Journal of Laser Applications 13 (2) (2001) 84–88.
[19] B.N. Chichkov, C. Momma, S. Nolte, F. von Alvensleben, A. Tünnermann, Femtosecond, picosecond and nanosecond laser ablation of solids, Applied Physics A Materials Science and Processing 63 (1996) 109–115.
[20] P.S. Banks, M.D. Feit, A.M. Rubenchik, B.C. Stuart, M.D. Perry, Material effects in ultra-short pulse laser drilling of metals, Applied Physics A Materials Science and Processing 69 (1999) S377–S380.
[21] H.K. Tönshoff, C. Momma, A. Ostendorf, S. Nolte, G. Kamiage, Microdrilling of metals with ultrashort laser pulses, Journal of Laser Applications 12 (1) (2000) 23–27.
[22] B. Le Drogoff, F. Vidal, Y. von Kaenel, M. Chaker, T.W. Johnston, S. Laville, Ablation of aluminum thin films by ultrashort laser pulses, Journal of Applied Physics 89 (12) (2001) 8247–8252.
[23] R. Le Harzic, N. Huot, E. Audouard, C. Jonin, P. Laporte, Comparison of heat-affected zones due to nanosecond and femtoseconds laser pulses using transmission electronic microscopy, Applied Physics Letters 80 (21) (2002) 3886–3888.
[24] B. Richerzhagen, Water-guided laser processing, Industrial Laser Review (1997) 8–10.
[25] Laser-Microjet—a new method for material processing, SYNOVA Report, Lausanne, Switzerland, 1998.
[26] U. Brinkman, Waterjet-Guided Laser Cuts Solar Cells, Laser Focus World, Pennwell Corporation in Nashua, NH, Adelaide, SA, September 1999.
[27] J.P. Holman, Heat Transfer, ninth ed., McGraw-Hill, New York, 2002.
[28] S.V. Patankar, Numerical Heat Transfer and Heat Flow, McGraw-Hill, New York, 1980.
[29] P. Schvan, R.E. Thomas, Time-dependent heat flow calculation of cw laser-induced melting of silicon, Journal of Applied Physics 57 (10) (1985) 4738–4741.
[30] C.P. Grigoropoulos, R.H. Buckholz, G.A. Domoto, A heat-transfer algorithm for the laser-induced melting and recrystalization of thin silicon layers, Journal of Applied Physics 60 (7) (1986) 2304–2309.
[31] B.W. Webb, C.-F. Ma, Single-phase liquid jet impingement heat transfer, Advances in Heat Transfer 26 (1995) 105–217.